Contemporary Mathematics

Singularity Formation in Free-Surface Stokes Flows

Qing Nie, Saleh Tanveer, Todd F. Dupont, and Xiaofan Li

Abstract. Two cases of evolution of interfaces in axi-symmetric Stokes flow are considered: 1) a bubble whose volume changes with time and 2) a viscous drop whose interior and exterior fluids have different viscosities. Direct numerical simulations for Stokes equations with moving boundaries are performed by using boundary integral formulations. It is found that, for the bubble with volumetric change, the surface can from (near) cusps or undergo topological changes (break-up of the surface). The dynamics of these bubbles are qualitatively similar to the exact solutions previously found in a two-dimensional study, and a self-similar process of pinching is observed. For a viscous drop surrounded by another viscous fluid, the interface develops a cone around the pinching region, the angles of the cone in this model agree with the physical experiments for a wide range viscosity ratios.

1. Introduction

Singularity formation in fluids is a challenging scientific problem of great technological importance. In particular the break-up of a bubble or a drop through topological changes has been a subject of considerable interest [**1**] [**2**] [**3**]. The understanding of detailed dynamics during break-up has application in practical situations such as in ink jet printers and disk atomizers.

Following the work by Lord Rayleigh [**4**] on the capillary instability of a viscous thread, there has been a great deal of research on bubbles and drops in a viscous flow [**5**] [**6**] [**7**] [**8**]. Most of the detailed studies of the dynamic break-up of drops have focused on the cases for which either the exterior fluid has zero viscosity or the viscosity ratio λ between the interior and exterior fluids is equal to one [**9**] [**2**] [**10**]. In this paper, we will investigate 1) the break-up of a Stokes bubble ($\lambda = 0$) and 2) the break-up of a drop of $\lambda \neq 1$.

For the first case, we are interested in the evolution of a Stokes bubble with volumetric change. A number of physical mechanisms can cause changes in bubble size. For instance, a bubble shrinks when the gas inside the bubble dissolves in the ambient liquid without significantly affecting the exterior fluid flow. In cases where the fluid inside the bubble is sufficiently compressible, a fluctuating pressure field imposed at infinity could alter bubble volume.

1991 *Mathematics Subject Classification.* Primary 76, 35; Secondary 65, 45.

For two-dimensional Stokes flow, analytical and numerical solutions have shown that, in general, a shrinking bubble forms cusps or near cusps, or it undergoes topological changes before its area reduces to zero [**11**] [**12**] [**13**]. A expanding bubble, on the other hand, is found to approach an expanding circle.

In the first part of the paper, we study the stability and singularity formation for an axi-symmetric bubble with volumetric change and compare its behavior with that of a 2-D bubble. A priori, the differences between two and three dimensions might be expected to have substantial effects on the observed phenomena. Our results suggest that while the quantitative the singularities associated with bubble pinching are different in 2-D and 3-D, the qualitative behavior is the same. Further, numerical calculation indicates that pinching is a locally self-similar process, and the similarity variables close to pinching are studied.

In the second part, we investigate the break-up of a Stokes drop for a range of viscosity ratios λ. Recently, Lister and Stone [**10**] studied break-up of a viscous thread surrounded by another viscous fluid. They found a self-similar pinching region through scaling arguments and numerical simulations of Stokes equations. In their study, the viscous thread is modeled by a potion of drop and the viscosity ratio is assumed to be one. Later, Cohen *et al.* [**14**] performed the physical experiments for drops with a range of viscosity ratios. They compared the experiments with the theory in [**10**] for the case with $\lambda = 1$, and found that the surface develops canonical cones at the pinch-off for all values of λ studied. In this paper, we perform numerical simulations of axi-symmetric Stokes flow for several cases of $\lambda \neq 1$. It is found that the angles of the cone around the pinch-off region of the viscous thread agree with the experiments [**14**] for large and medium-sized λ, however there are some discrepancies for very small λ.

The paper is organized as follows: The equations and boundary integral formulations of the free-surface motion are presented in Section 2. The numerical methods for solving the equations are briefly discussed in Section 3. A linear stability analysis of an arbitrary contracting or expanding spherical bubble, and numerical results of the evolution of a bubble and a viscous thread are shown in Section 4. A summary is presented in Section 5.

2. Equations and Boundary Integral Formulations

2.1. A Stokes Bubble with Volumetric Change. In low Reynolds number limit, the flow outside the bubble satisfies the Stokes equation and the continuity equation

$$\mu \nabla^2 \mathbf{u} = \nabla p \qquad \text{and} \qquad \nabla \cdot \mathbf{u} = 0, \tag{1}$$

where $\mathbf{u}$ is the fluid velocity, p is the fluid pressure and μ is the fluid viscosity. We consider the situation in which the bubble surface is the only boundary and suppose that

$$\mathbf{u} \to 0 \qquad \text{as} \qquad \mathbf{x} \to \infty, \tag{2}$$

The stress on the bubble surface S is balanced by the interfacial tension force as

$$\mathbf{T} \cdot \mathbf{n} = \tau(\nabla \cdot \mathbf{n})\mathbf{n}, \tag{3}$$

where $\mathbf{T} = -p\mathbf{I} + \mu\left[\nabla\mathbf{u} + (\nabla\mathbf{u})^T\right]$, $\mathbf{n}$ is the unit outward normal at the bubble boundary and τ is the surface tension. The interfacial kinematic condition requires

$$\frac{d\mathbf{x}}{dt} \cdot \mathbf{n} = \mathbf{u} \cdot \mathbf{n} \qquad \text{on } S \tag{4}$$

Finally, the volume of the bubble is required to change at a constant prescribed nonzero rate A, i.e.

$$\int_S \mathbf{u} \cdot \mathbf{n} dS = A. \tag{5}$$

We use L, the radius of the initial bubble, as the length scale, $|A|/L^2$ as the velocity scale. The pressure is non-dimensionalized by $\mu|A|/L^3$, and the time scale is chosen as $L^3/|A|$. Therefore,the equations contain only one non-dimensional parameter,

$$G = \frac{\tau L^2}{\mu|A|}. \tag{6}$$

With this non-dimensionalization, the rate of change of non-dimensional bubble volume is either 1 or -1, corresponding to an expanding or a contracting bubble, respectively. Henceforth, all physical variables are considered non-dimensional.

The numerical method, which we use to follow the evolution of an axi-symmetric bubble, is based on a boundary integral formulation for solving Stokes equations with a moving boundary [**15**] [**5**] [**16**]. The velocities of the bubble surface satisfy the Fredholm integral equation of the second kind,

$$u_j(\mathbf{x}) + \fint_S u_i(\mathbf{y}) K_{ijk}(\mathbf{x},\mathbf{y}) n_k(\mathbf{y}) dS(\mathbf{y}) = f_j(\mathbf{x}) \tag{7}$$

where

$$K_{ijk}(\mathbf{x},\mathbf{y}) = \frac{3}{2\pi} \frac{(y_i - x_i)(y_j - x_j)(y_k - x_k)}{|\mathbf{y} - \mathbf{x}|^5} \tag{8}$$

$$f_j(\mathbf{x}) = \left(\int_S (\nabla \cdot \mathbf{n}(\mathbf{y})) n_i(\mathbf{y}) J_{ij}(\mathbf{x},\mathbf{y}) dS(\mathbf{y}) \right) G \tag{9}$$

$$J_{ij}(\mathbf{x},\mathbf{y}) = -\frac{1}{4\pi} \left(\frac{1}{|\mathbf{y} - \mathbf{x}|} + \frac{(y_i - x_i)(y_j - x_j)}{|\mathbf{y} - \mathbf{x}|^3} \right) \tag{10}$$

$\mathbf{J}$ and $\mathbf{K}$ are the Green's functions for the velocity and stress fields, respectively. P indicates the principal-value integral. Equation (5) implies that

$$\int_S u_i(\mathbf{y}) n_i(\mathbf{y}) dS(\mathbf{y}) = \mathrm{sgn}(A). \tag{11}$$

The eigenvalue problem for the homogeneous equation associated with (7) has an eigenvalue one with multiplicity one. For (7) to have a solution, f_j must satisfy the Fredholm alternative condition. Note that the corresponding adjoint problem is

$$w_j(\mathbf{x}) + n_k(\mathbf{x}) \fint_S w_i(\mathbf{y}) K_{jik}(\mathbf{y},\mathbf{x}) dS(\mathbf{y}) = 0. \tag{12}$$

It is easy to check that $w_j(\mathbf{x}) = n_j(\mathbf{x})$ is the eigenfunction of (12) by using the identity

$$\fint_S K_{ijk}(\mathbf{x},\mathbf{y}) n_j(\mathbf{x}) dS(\mathbf{x}) = -\delta_{ik}. \tag{13}$$

Also, it can be shown that

$$\int_S f_i(\mathbf{y}) n_i(\mathbf{y}) dS(\mathbf{y}) = 0 \tag{14}$$

by using

$$\int_S J_{ji}(\mathbf{x},\mathbf{y}) n_i(\mathbf{x}) dS(\mathbf{x}) = 0. \tag{15}$$

Thus f_j indeed satisfies the Fredholm alternative condition. The arbitrary constant in the solution of (7) corresponds to the freedom of choice of bubble volume. By demanding (11), a unique solution to (7) can be obtained. In fact (7) and (11) can be combined into one equation as

$$\begin{aligned} & u_j(\mathbf{x}) + \fint_S u_i(\mathbf{y}) K_{ijk}(\mathbf{x},\mathbf{y}) n_k(\mathbf{y}) dS(\mathbf{y}) \\ = \;& f_j(\mathbf{x}) + n_j(\mathbf{x}) \left(\int_S u_i(\mathbf{y}) n_i(\mathbf{y}) dS(\mathbf{y}) - \mathrm{sgn}(A) \right). \end{aligned} \tag{16}$$

It is clear that (7, 11) itself implies (16). We now show that (16) implies (7, 11). We multiply (16) by $n_j(\mathbf{x})$ and integrate over S, the left-hand side of (16) vanishes by using (13), and the first term on the right vanishes due to (15). Consequently, we obtain equation (11). From (16, 11), clearly (7) follows. The advantage in having equations in the form (16) is that the resulting integral equation has a unique solution for u_j.

2.2. Dynamics of a Viscous Drop. Consider the dynamics of a Stokes drop of viscosity μ_1, density ρ_1, and surface tension γ in a surrounding fluid of viscosity μ_2 and density ρ_2. Let the drop surface S have outward normal $\mathbf{n}$ so that the flow is driven by a capillary jump in stress $\gamma(\nabla \cdot \mathbf{n})\ \mathbf{n}$ across S. We make all velocities dimensionless with respect to the scale γ/μ_2 and use the initial radius of the drop for length scales. Denote the viscosity ratio $\lambda = \mu_1/\mu_2$. The velocity $u_j(x)$ on S has the following boundary integral representation [**5**] [**16**]:

$$\begin{aligned} u_j(\mathbf{x}) \;+\; & \frac{1-\lambda}{1+\lambda} \fint_S u_i(\mathbf{y}) K_{ijk}(\mathbf{x},\mathbf{y}) n_k(\mathbf{y}) dS(\mathbf{y}) \\ = \;& \frac{1}{1+\lambda} \int_S (\nabla \cdot \mathbf{n}(\mathbf{y})) n_i(\mathbf{y}) J_{ij}(\mathbf{x},\mathbf{y}) dS(\mathbf{y}) \end{aligned} \tag{17}$$

The drop surface S then is updated using the equation (4).

3. Numerical Method

When the flow is assumed to be axi-symmetric, the surface integrals can be reduced to line integrals by performing the azimuthal integration analytically. The resulting complete elliptic integrals of the first and second kind can computed by recursive formulae [**17**].

The numerical technique of solving the system of equations is similar to those studied in [**16**] [**18**]. First of all, the free surface S is approximated by a set of boundary nodes along the contour in the (r, z) meridional plane. The boundary integral equation (16) or (17) is solved using a collocation method. The principal integrals are first de-singularized using simple integral identities [**16**] and approximated by six-point Gaussian quadratures. The position at the quadrature points is

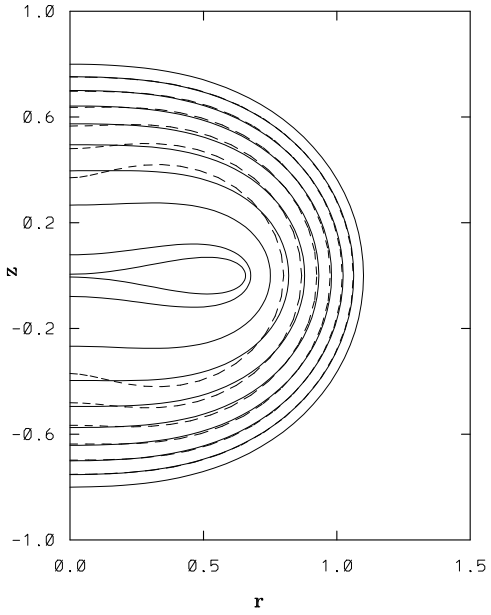

FIGURE 1. Comparison between the numerical solutions (the solid curves) and the linear solutions (the dotted ones) for a contracting bubble with $G = 0.02$. The initial shape is given by (37) and (38) with $\epsilon = -0.3$. The solid curves correspond to the axi-symmetric bubble profiles in the (z, r)-plane at times $t = i\times 0.5, i = 0, ..., 8$ and $t = 4.15$ while the dotted ones are associated with $t = i \times 0.5, i = 1, ..., 6$.

obtained by quintic spline interpolation based on the corresponding position of the nodes [**19**]. The resulting linear systems from the discretization of the boundary integral equations are solved using iterative procedures such as GMRES [**20**]. To accelerate convergence of the iteration, the initial guess for the iteration procedure at each time step is obtained by a fourth-order extrapolation from solutions at earlier time steps.

Once the velocity of free surface is calculated the free surface is advanced according to (4). The time integration is carried out using a fourth-order Adams-Moulton predictor-corrector scheme with the starting values obtained through a fourth-order Runge-Kutta scheme. All computations are performed using 64-bit arithmetic.

4. Results

4.1. Linear Stability for a Stokes Bubble with Volumetric Change. A trivial solution to (1-6) is a contracting or expanding spherical bubble. In the spherical polar coordinates (R, θ, ϕ), with the assumption of axi-symmetry, the bubble interface may be represented as $R = \mathcal{R}(\theta, t) = R_0(t)$. The two components of the velocities are

$$\bar{u}_R(R, \theta, t) = \frac{R_0^2 \dot{R}_0}{R^2} \qquad \bar{u}_\theta(R, \theta, t) = 0, \tag{18}$$

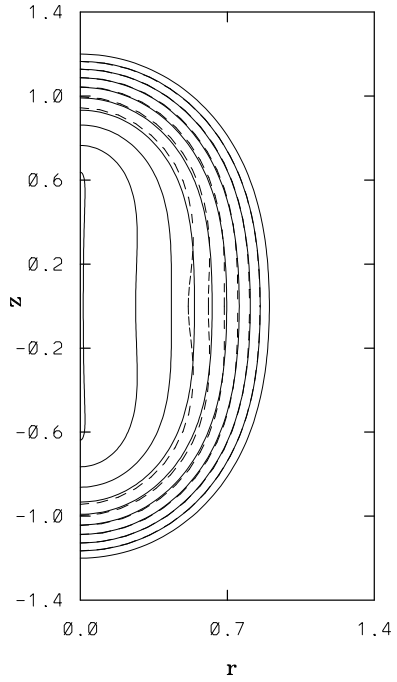

FIGURE 2. Comparison between the numerical solutions (the solid curves) and the linear solutions (the dotted ones) for the same conditions described in Figure 1 except $\epsilon = 0.3$. The solid curves are plotted at times $t = i \times 0.5, i = 0, ..., 8$ and $t = 4.29$ while the dotted ones at $t = i \times 0.5, i = 1, ..., 6$.

and the pressure is

$$\bar{p}(R, \theta, t) = p_\infty(t) = -2\left(2\frac{\dot{R}_0}{R_0} + \frac{G}{R_0}\right) \tag{19}$$

$R_0(t)$ is determined by

$$\frac{d}{dt}\left(\frac{4\pi}{3}R_0^3(t)\right) = \text{sgn}(A). \tag{20}$$

where $\text{sgn}(A) = 1$ for $A > 0$ and $= -1$ for $A < 0$. However, the results of the linear stability analysis prescribed in this section transcend the restriction (20) on $R_0(t)$ and can be applied to any spherical bubble with specified radius $R_0(t)$. Therefore, the restriction (20) will not be imposed in this section.

We are now in a position to analyze the evolution of small axi-symmetric perturbations on a spherical bubble. The analysis is similar in spirit to any linear stability analysis on a spherical bubble, such as [**21**] except that unlike previous cases, the bubble volume is changed. Since Legendre polynomials, $\{P_k(\cos(\theta))\}_{k=0}^{\infty}$, form a complete set in describing any function of θ, it is enough to consider bubble shape perturbations in the form

$$R = \mathcal{R}(\theta, t) = R_0(t)\left(1 + \epsilon\rho(t)P_k(\cos(\theta))\right) + O(\epsilon^2), \tag{21}$$

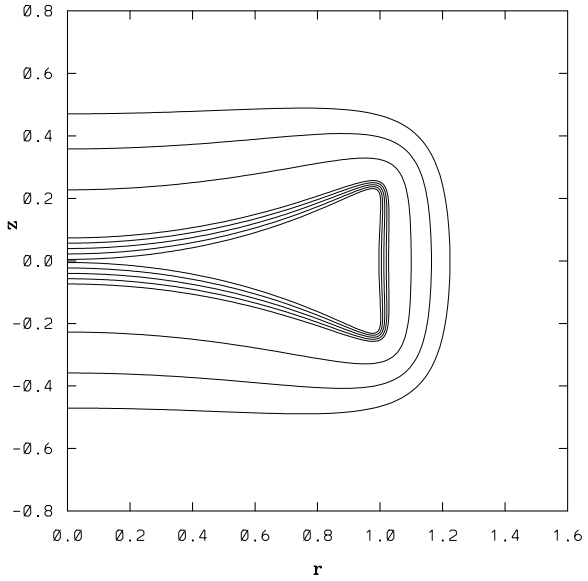

FIGURE 3. The evolution of a bubble surface for initial condition (39) with $G = 0$ at $t = (i-1), i = 1, ..., 4$, and $t = 3 + i \times 0.1, i = 1, ..., 4$.

where ϵ is a small constant. It is easily seen that the corresponding velocities must take the form,

$$u_R(R,\theta,t) = \bar{u}_R + \epsilon U(R,t) P_k(\cos(\theta)) + O(\epsilon^2) \tag{22}$$

$$u_\theta(R,\theta,t) = \epsilon W(R,t) \sin(\theta) P_k^{'}(\cos(\theta)) + O(\epsilon^2) \tag{23}$$

while pressure is

$$p(R,\theta,t) = \bar{p} + \epsilon q(R,t) P_k(\cos(\theta)) + O(\epsilon^2). \tag{24}$$

For disturbances not affecting the volume, it is clear that the $k = 0$ mode needs to be excluded. So we will assume $k \geq 1$. Substituting (21-24) into the equations of motion (1-4), we obtain the linearized Stokes and continuity equations:

$$-\frac{\partial q}{\partial R} + \frac{\partial^2 U}{\partial R^2} + \frac{2}{R}\frac{\partial U}{\partial R} - \frac{k^2+k+2}{R^2}U - \frac{2k(k+1)}{R^2}W = 0, \tag{25}$$

$$\frac{q}{R} + \frac{\partial^2 W}{\partial R^2} + \frac{2}{R}\frac{\partial W}{\partial R} - \frac{k(k+1)}{R^2}W - \frac{2U}{R^2} = 0, \tag{26}$$

$$\frac{\partial U}{\partial R} + \frac{2}{R}U + \frac{k(k+1)}{R}W = 0. \tag{27}$$

Linearization of normal and tangential components of stress about $R = R_0(t)$ results in the following $O(\epsilon)$ equations:

$$q - 2\left(\frac{6\dot{R}_0}{R_0}\rho(t) + \frac{\partial U}{\partial R}\right) + G\frac{\rho(t)}{R_0}(k+2)(k-1) = 0 \qquad \text{at } R = R_0(t), \tag{28}$$

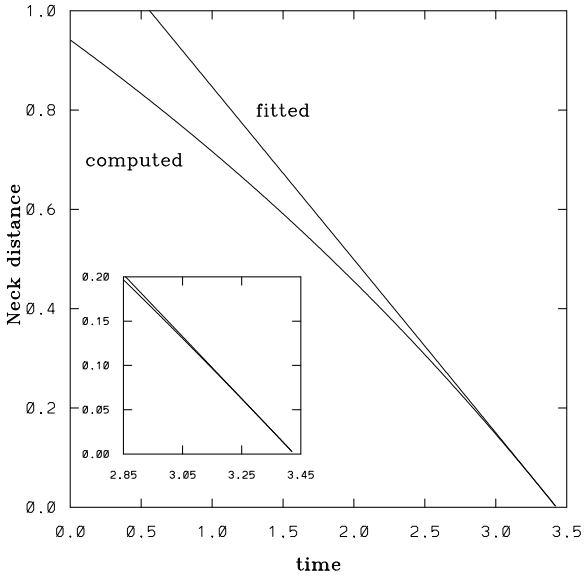

FIGURE 4. The neck distance vs. time for initial condition (39) with $G = 0$.

(29)
$$3\dot{R}_0\frac{\rho(t)}{R_0} - \frac{1}{2}\left\{\frac{U}{R_0} + \frac{1}{k(k+1)}\left(R_0\frac{\partial^2 U}{\partial R^2} + 2\frac{\partial U}{\partial R} - \frac{2}{R_0}U\right)\right\} = 0 \qquad \text{at } R = R_0(t),$$

while the $O(\epsilon)$ kinematic equation is

$$\dot{\rho}(t) = \frac{U}{R_0} - 3\rho\frac{\dot{R}_0}{R_0} \qquad \text{at } R = R_0(t). \tag{30}$$

After eliminating W and q among (25-27), we obtain

$$\begin{aligned} & R^2\frac{\partial^4 U}{\partial R^4} + 8R\frac{\partial^3 U}{\partial R^3} + (12 - 2k(k+1))\frac{\partial^2 U}{\partial R^2} \\ - \quad & \frac{4k(k+1)}{R}\frac{\partial U}{\partial R} + k(k+1)(k^2+k-2)\frac{U}{R^2} = 0. \end{aligned} \tag{31}$$

The general solutions of (31) are

$$U(R,t) = \frac{a_0(t)}{R^k} + \frac{a_1(t)}{R^{k+2}} + a_2(t)R^{k-1} + a_3(t)R^{k+1} \tag{32}$$

where $a_i(t), i = 0, ..., 3$ are as yet undetermined. Since $k \geq 1$, the relation (2) implies $a_2(t), a_3(t) = 0$. From (26, 27), it follows that

$$W(R,t) = \frac{1}{k(k+1)}\left(\frac{ka_1}{R^{k+2}} - \frac{(2-k)a_0}{R^k}\right) \tag{33}$$

$$q(R,t) = \frac{2(2k-1)}{k+1}\frac{a_0}{R^{k+1}} \tag{34}$$

Finally, we use (32-34) in (28, 29) with $a_2 = 0 = a_3$ to eliminate a_0 and a_1 in terms of ρ. Using these resulting expressions in (30), we obtain a first order ODE

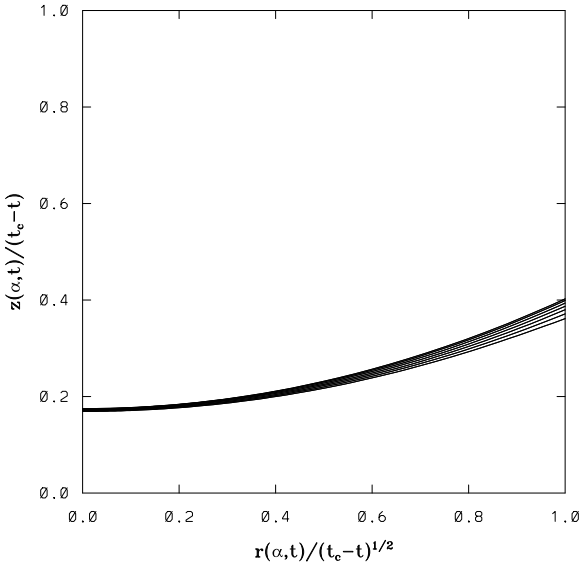

FIGURE 5. Local behavior of $F(y)$ near $y = 0$ for initial condition (39) with $G = 0$

for $\rho(t)$ which is readily integrated to give

$$\rho(t) = \rho(0)\left(\frac{R_0(0)}{R_0(t)}\right)^{\frac{3k(2k-1)}{(2k^2+1)}} \exp\left\{-G\frac{(2k+1)(k^2-1)}{2(2k^2+1)}\int_0^t \frac{ds}{R_0(s)}\right\} \tag{35}$$

Notice that the surface tension correction factor is 1 for $k = 1$. For any fixed $k > 1$, this correction is small for small G unless $\int_0^t R_0^{-1}(s)ds$ is large. Also, any non-zero G is seen to stabilize disturbances corresponding to sufficiently large k. It is clear from (35) that the spherical solution is unstable when $R_0(t)$ decreases, i.e. for a contracting bubble; on the other hand, it is stable when $R_0(t)$ increases for an expanding bubble. In essence, the sign of A, sgn(A), determines the linear stability. For the case of constant rate of volume change according to (20), $R_0(t)$ appearing in (35) has to be replaced by

$$R_0(t) = \left(1 + \frac{3\text{sgn}(A)}{4\pi}t\right)^{\frac{1}{3}}. \tag{36}$$

4.2. Numerical Studies for a Stokes Bubble with Volumetric Change. First of all, we compare the numerical solutions with those from the linear stability analysis in Section 2. Consider the following initial condition

$$r(\theta) = R(\theta)\sin(\theta) \qquad z(\theta) = R(\theta)\cos(\theta) \tag{37}$$

where

$$R(\theta) = 1 + \epsilon\rho(0)P_k(\cos(\theta)) + \epsilon^2 d \tag{38}$$

with d chosen to ensure that the initial volume of the bubble is $\frac{4}{3}\pi$. Also we set $\rho(0) = 1$ without loss of generality.

From linear stability analysis, for sgn$(A) = 1$ any small disturbance on the bubble surface should decrease to zero. This is found to be true for the nonlinear

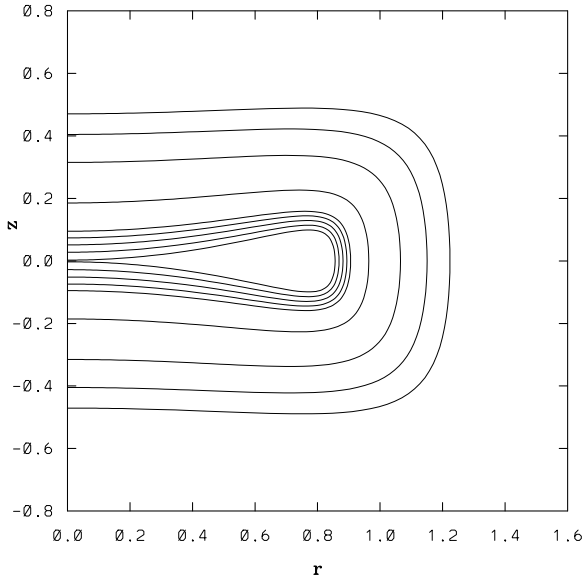

FIGURE 6. The evolution of a bubble surface for initial condition (39) with $G = 0.1$ at $t = (i-1)$ for $i = 1, ..., 4$, and $t = 3.4 + i \times 0.1$ for $i = 1, ..., 5$.

numerical solutions for ϵ ranging from small to order one. For $\text{sgn}(A) = -1$, the bubble surface evolves away from a sphere for small perturbations. The evolution of the bubble is plotted in Figure 1 for $G = 0.02$ and an initial condition: $k = 2$, and $\epsilon = -0.3$ in (38). The linear solutions and the numerical solutions agree well until the bubble evolves significantly away from a sphere around $t = 2$. The nonlinear effect slows down the contracting of the surface around $r = 0$. Notice that at later time, as shown Figure 1, in the three-dimensional bubble shape is similar to that of a dimpled pancake.

In Figure 2, we plot the evolution of a bubble with an initial condition: $k = 2$ and $\epsilon = 0.3$. The other parameters are chosen to be the same as in Figure 1. Similar to Figure 1, the nonlinear and linear solutions agree well at early times, and the nonlinear effect tends to slow down the pinch-off of the bubble. However, the three-dimensional shape of the bubble in Figure 2 at later time resembles a peanut shape, in contrast to a dimpled pancake in Figure 1. In other words, the bubble surface collapses onto $z = 0$ plane for the case depicted in Figure 1 while the surface shrinks onto the z-axis for the case in Figure 2. As shown later, these two pinching processes behave differently.

The computations for Figure 1 and 2 have to be stopped due to the loss of the resolution when the bubble surface comes close to pinching. For a boundary integral method, the accuracy of calculation deteriorates when two parts of the interface approach each other. For an accurate calculation of the principal integrals, it is necessary to maintain a large value of ζ, which is defined as the ratio of the smallest distance between the two parts of the bubble surfaces over the distance between the neighboring nodes closest to the pinching point on the same side of the surface.

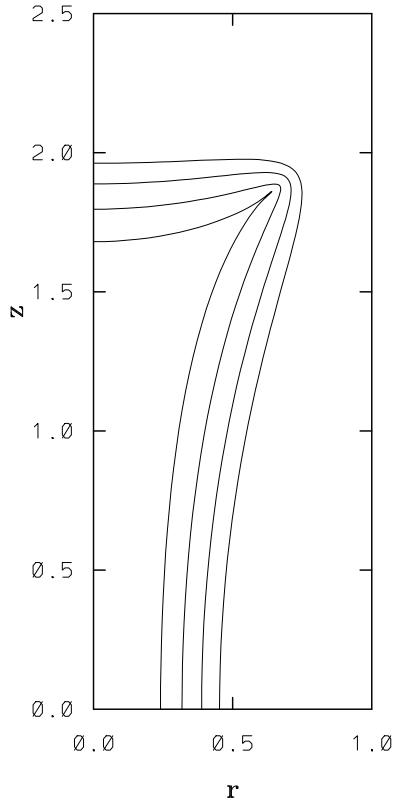

FIGURE 7. The evolution of a bubble surface for initial condition (46) with $G = 0$ at $t = (i-1)$ for $i = 1, ..., 4$.

Computation has to be stopped when ζ fails to be sufficiently large, as is the case when pinching is approached.

In order to study the detailed behavior of the bubble surface near pinch-off, we start with initial bubble surfaces that resemble later time profiles in Figures 1 and 2. By doing this, we can choose a surface parameterization that concentrates points around the pinching-off areas.

In particular, for the case of a dimpled pancake we choose

$$r(\nu) = (b-a)\sin(\nu) + c\,\sin(3\nu) \qquad z(\nu) = (b+a)\cos(\nu) + c\,\cos(3\nu) \tag{39}$$

where $a = -d$, $b = 0.4d$, $c = 0.1d$, with the constant d chosen to ensure that the initial volume of the bubble is $\frac{4}{3}\pi$. Further, we use a stretching transformation

$$\nu = \alpha - 0.5\gamma\,\sin(2\alpha), \tag{40}$$

where $\gamma = 0.8$. For equally spacing α, the collocation points generated by (39, 40) cluster near $r = 0$ initially, and it is found that they remain clustered near pinching as time advances. With this parameterization (40), it is possible to calculate the surface evolution more accurately around pinching than the calculation shown in Figure 1.

In Figure 3, it shows the evolution of a bubble subjected to the initial condition (39) with $G = 0$. The bubble surface comes close to pinching well before the bubble

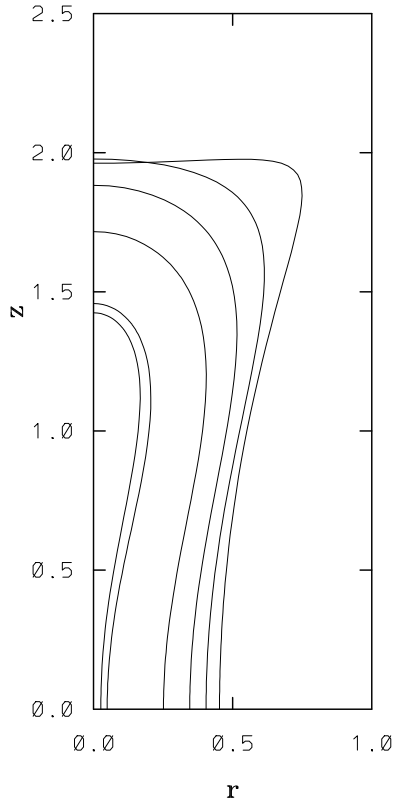

FIGURE 8. The evolution of a bubble surface for initial condition (46) with $G = 0.5$ at $t = (i-1)$ for $i = 1, ..., 5$, and $t = 4.06$.

volume becomes zero. In this case, $N = 257$ and $\triangle t = 0.0025$ are used for the calculation. The error tolerance for solving the integral equation (16) is set to 10^{-10}, and the typical iteration number in GMRES is 9 and it increases to as many as 30 as the bubble surface is near pinch-off. Resolution studies in space and time, as well as the error in volume of bubble have been shown in [**22**].

We now turn to investigating a possible self similar process describing pinching. For this initial condition, we assume a self-similar relationship near pinch-off:

$$z(\alpha, t) \sim (t_c - t)^p \, F\left(\frac{r(\alpha, t)}{(t_c - t)^q}\right). \tag{41}$$

with $q > 0$. To obtain p, q and t_c, we fit the numerically calculated $z(0, t)$ and $z_{\alpha\alpha}(0, t)$ to the following forms,

$$z(0, t) \sim (t_c - t)^p F(0); \tag{42}$$

$$z_{\alpha\alpha}(0, t) \sim (t_c - t)^{p-2q} F^{''}(0) r_\alpha^2(0, t_c). \tag{43}$$

Numerically, $r_\alpha(0, t_c)$ is found to be nonzero. Now we briefly describe the procedure for estimating p, q and t_c. First we apply a nonlinear least square fit to (42) over M (> 3) consecutive points in time to determine p, t_c and $F(0)$. Once p is determined, q is determined from using (43) over two adjacent time steps. The

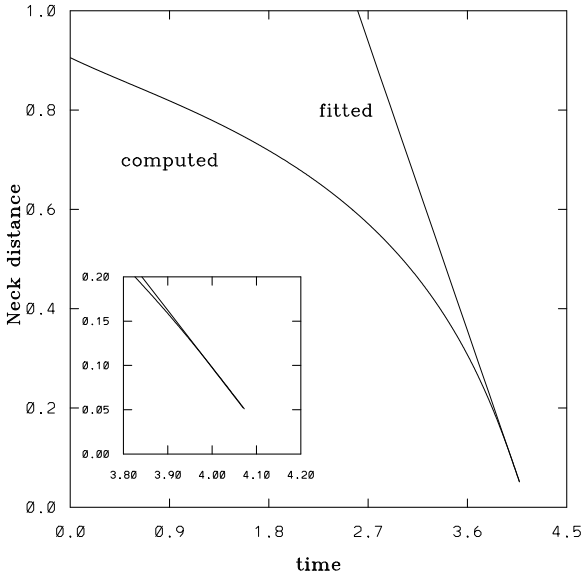

FIGURE 9. The neck distance vs. time for initial condition (46) with $G = 0.5$.

N	t_f	t_c	p	q	$F(0)$	deviation
33	3.25	3.4245	0.9684	0.5119	0.1692	$9{,}2\times10^{-8}$
65	3.35	3.4271	0.9837	0.5041	0.1714	1.7×10^{-7}
129	3.40	3.4277	0.9913	0.5004	0.1732	3.8×10^{-6}
257	3.415	3.4283	0.9966	0.4997	0.1746	5.4×10^{-6}

TABLE 1. The estimation of p, q, t_c for (39) and different N using 30 time steps

largest time t_f used for the purpose of this fit depends on the estimated accuracy of the solutions. As measured by comparing with higher resolution, the accuracy of the solution close to pinching depends on the ratio ζ of the neck distance over the local spacing. In the computation, we require that both $\zeta > 2$ and the spatial accuracy $< 10^{-4}$. One of these criteria fails for the first time past $t = t_f$. We define "deviation" in Tables 1 and 2 as the least square error, corresponding to the estimated p, t_c and $F(0)$. In Table 1, p, q , t_c, $F(0)$, t_f and deviation are shown for different N, where $M = 30$, i.e. 30 pairs of consecutive values $(t_i, z(0, t_i))$ are used to compute the least square with $t_i = t_f - (i-1) \times 0.0025, i = 1...30$. Similarly in Table 2, the first 15 pairs of values from the computation in Table 1 is employed. The convergence of the computed p, q, t_c and $F(0)$ is easily observed from both tables and the results indicate consistency between $M = 15$ and 30. Up to three digit precision, we determine $p = 1$, $q = 1/2$, $t_c = 3.428 \pm 10^{-3}$, and $F(0) = 0.174 \pm 10^{-3}$.

To check the consistency of the form-fit, both computed neck distance of the bubble as well as the the right-hand side of (42), denoted as the "fitted" in Figure 4, are plotted as functions of the time. Both curves agree with each other very well when $t > 3$ (see the close-up). To check if indeed the similarity hypothesis (41) for

N	t_f	t_c	p	q	$F(0)$	deviation
33	3.25	3.4251	0.9712	0.5133	0.1695	8.6×10^{-8}
65	3.35	3.4274	0.9863	0.5054	0.1719	1.6×10^{-7}
129	3.40	3.4279	0.9940	0.5015	0.1742	6.5×10^{-6}
257	3.415	3.4283	0.9972	0.5000	0.1749	4.3×10^{-6}

TABLE 2. The estimation of p, q, t_c for (39) and different N using 15 time steps

t close to t_c is valid, $z(\alpha,t)/(t_c-t)$ is plotted as a function of $r(\alpha,t)/(t_c-t)^{\frac{1}{2}}$ at $t = 2.7 + 0.1\times i$ for $i = 1, ..., 7$ in Figure 5. The upper curves correspond to later times. Note that $t = 3.3, 3.4$ curves are almost on top of each other as is expected if (41) is valid for t approaching t_c.

Adding surface-tension has no significant effect on the pinching behavior for this case because curvature is small near the pinching point. As shown in Figure 6, which has the same initial condition as in Figure 3 but $G = 0.1$, the bubble breaks up as in Figure 3. A similar study demonstrates that $p = 1$, $q = \frac{1}{2}$, $t_c = 3.911\pm10^{-3}$, and $F(0) = 0.247 \pm 10^{-3}$ for this case. The neck distance as a function of time, and the local behavior of $F(y)$ are similar to those in Figures 4 and 5 [**22**]. They are not shown here.

The results in the case of an initial dimpled pancake is not surprising because the surface pinches as $z \to 0$. In other words, the fluid on top and bottom of the bubble are "unaware" of each other as they are drawn together by the global condition of volume reduction. This is similar to the 2-D case [**11**] [**12**]. The pinching is consistent with a local quadratic behavior

$$z \sim a_0 r^2 + b_0(t_c - t) \tag{44}$$

which implies

$$\frac{z}{t_c - t} \sim a_0 \left(\frac{r}{(t_c-t)^{\frac{1}{2}}}\right)^2 + b_0 \tag{45}$$

This is consistent with (42) with $p = 1$ and $q = \frac{1}{2}$. Confirmation of this result suggests the reliability of the form-fit and indirectly the accuracy of the numerics, even close to pinching.

We turn now to studying another set of initial condition.

$$r(\nu) = (b+a)\sin(\nu) - c\,\sin(3\nu) \qquad z(\nu) = (a-b)\cos(\nu) + c\,\cos(3\nu) \tag{46}$$

where $a = -d$, $b = 0.5d$, $c = 0.2d$, and d is a constant such that the initial volume of the bubble is $\frac{4}{3}\pi$. This initial bubble, unlike the previous case, has the shape of a peanut and qualitatively resemble the $t = 4$ curve in Figure 2. The evolution of a bubble (only half of the profile plotted) for $G = 0$ is shown in Figure 7. Here the bubble surface develops a cusp, within numerical precision. Such cusps have been observed earlier for exact 2-D solutions in [**11**]. In that case a small nonzero surface tension smoothes out the cusp locally, but the shapes are near cusps. This is expected for the axi-symmetric case as well for small G, though numerically calculation becomes difficult. Not surprisingly, when $G = 0.5$, the cusp formation with initial condition (46) is smoothed out over a large scale. The bubble then tends to pinch at the origin as seen in Figure 8. In order to better resolve the pinching, we

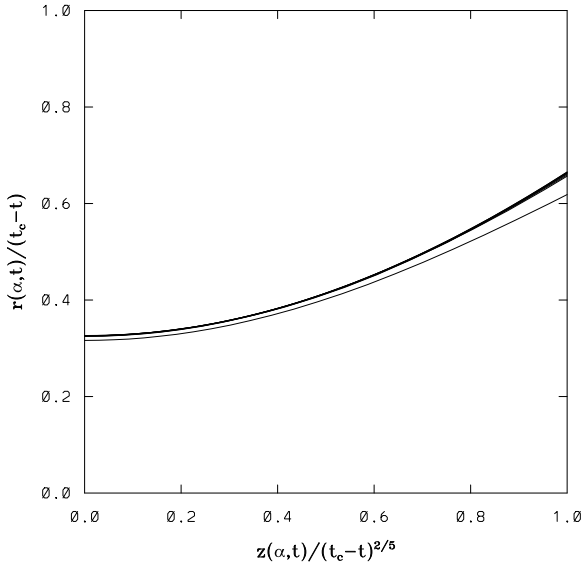

FIGURE 10. Local behavior of $F(y)$ near $y = 0$ for initial condition (46) with $G = 0.5$.

N	t_f	t_c	p	q	$F(0)$
129	4.050	4.1495	0.9828	0.3988	0.3175
257	4.060	4.1508	0.9921	0.4000	0.3234

TABLE 3. The estimation of p, q, t_c for (46) and different N

cluster the collocation points around $z = 0$ initially by choosing uniformly spaced points in α and choosing

$$\nu = \alpha + 0.5\gamma \sin(2\alpha), \tag{47}$$

with $\gamma = 0.8$.

Before proceeding with discussion of the pinching behavior, we remind the reader once again about the essential difference between the two initial conditions (39) and (46). Although both initial bubble shapes look similar in the meridional plane with r and z interchanged, their actual 3-D shapes are significantly different as discussed above (one is pancake shaped and the other resembles a peanut). ¿From a computational point view, the second case provides more numerical difficulties due to the presence of term $1/r$ in the curvature, which is sensitive to round-off and computational errors as r approaches 0. Next we show a preliminary study to investigate a possible self-similar pinching process.

As in the previous case, the self similar form (41) is assumed, except that r and z are interchanged. In order to keep errors acceptable ($< 10^{-4}$), it is found that we need $\zeta > 5$. Since there are not enough available time steps near pinching where asymptotic behavior (41) is valid, we abandon the least square fit approach in favor of a direct fit to (42).

Specifically, we enforce (42) at three adjacent time steps ending at t_f, and solve the nonlinear equations through Newton iteration to obtain p, t_c and $F(0)$. The

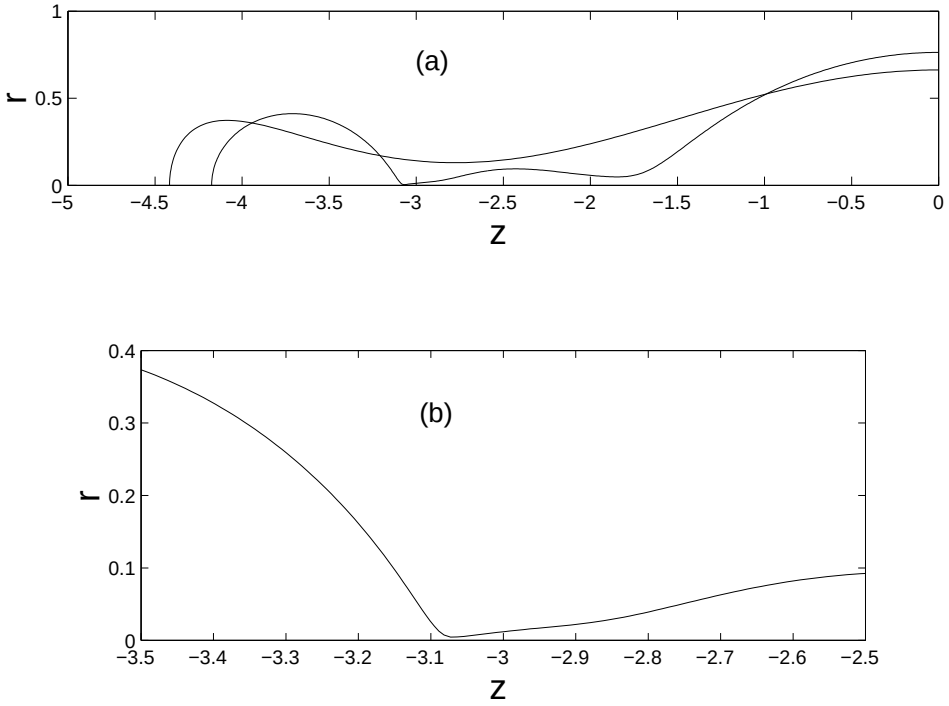

FIGURE 11. Profiles of a drop for $\lambda = 0.1$. (a) Initial and final (at pinch-off) shapes of half of a drop; (b) Close-up near pinch-off.

computation of q is similar to the previous case. In Table 3, a estimate of p, q, and t_c are given. The difference between the two solutions $N = 129$ and $N = 257$ agree up to 10^{-4} at $t = 4.06$, and the volume of the bubble is accurate to 10^{-6} for $N = 129$ and 10^{-8} for $N = 257$ respectively.

Based on the data in Table 3, we estimate that $p = 1$, $q = 2/5$, $t_c = 4.15 \pm 10^{-2}$ and $F(0) = 0.32 \pm 10^{-2}$. In Figure 9 and Figure 10, graphs similar to Figures 4 and 5 are shown for this initial condition (46) . In Figure 10, the bottom curve corresponds to $t = 3.9$ while all other curves overlap corresponding to $t = 4.0 + (i-1) \times 0.01$ for $i = 1, ..., 7$. We note different similarity exponent in this case compared to the previous case.

An analytic similarity solution describing this pinching appears to be difficult as the far-field behavior must come into play since the fluid velocity and pressure at any part of the interface is globally dependent on values at other parts of the interface. For instance, it is known within the context of 2-D Stokes flow that the interface between a zero viscosity fluid displacing a viscous fluid can be stable for an expanding inviscid bubble [**11**] or unstable for a contracting viscous blob [**23**]. This observation suggests that the far-field plays a very important role on the similarity process; and this makes it difficult to obtain a locally self-similar analytic solution. Further computational and analytic studies are in progress [**24**].

4.3. Numerical Studies for Pinch-off of a Viscous Drop. When a fluid droplet breaks, a singularity develops due to the infinite curvature at the point

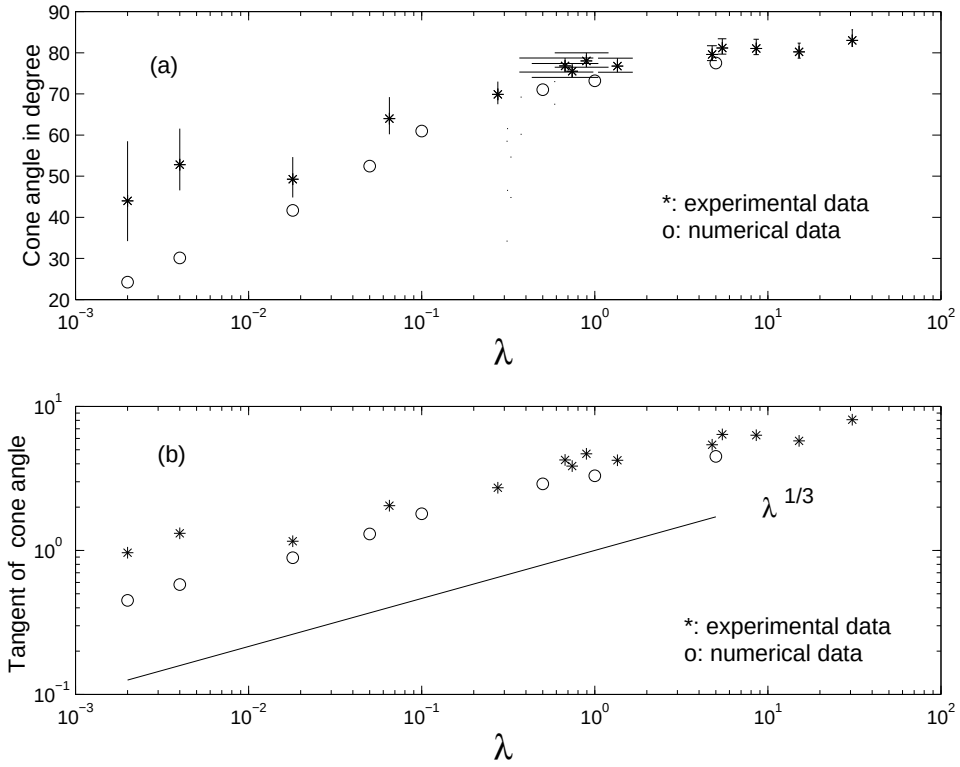

FIGURE 12. The large angle of the cone as a function of λ. (a) the angles in degree; (b) the tangent of the angles.

of pinch-off. For a viscous drop surrounded by another viscous fluid, physical experiments [**14**] indicate that two canonical cones meet at the pinch-off point, and the sizes of the two angles of the cones are independent of the initial shape of the droplet and depend only on the viscosity ratio of the interior and exterior fluids of the drop: λ.

In this work, we compute the numerical solutions of (17) in an axi-symmetric geometry for different values of λ. We choose an initial condition similar to the one in [**10**]. Figure 11 shows the calculation for $\lambda = 0.1$, in which the drop is represented by 1025 points. In Figure 11 (a), the initial shape of the drop and the final shape of the drop near pinching are plotted for half of the drop. Notice that the radial direction r is chosen to be vertical for convenience of presentation. Figure 11 (b) shows a close-up near pinch-off. As seen in the figure, locally near the pinch-off the drop develops a cone of a larger angle on the left and a cone of smaller angle on the right.

In order to estimate the angles of the cone, we first extrapolate a temporal sequence of the profiles of the drop surface to estimate the pinch-off time and location. Next we estimate the angles at several time-steps before pinch-off using various portions of the surface. Then we extrapolate the obtained angles to obtain the cone angles at the pinch-off. For $\lambda = 1$, the sizes of the two angles are found

consistent with those in [**10**]. However, we notice that angle of the small cone is more prone to numerical errors and more difficult to estimate than the larger one.

In Figure 12, we display the larger cone angles obtained from our numerical simulations and the physical experiments in [**14**] for different values of λ. The numerically estimated angles are consistently smaller than the experimentally estimated angles. However, for $\lambda \geq 0.018$, the numerical values are within or close to the error bars of those physical ones, and the agreement is better for larger values of λ. For the two smallest $\lambda = 0.002, 0.004$, it is clear that the numerical result does not agree with the experiments. It is interesting to notice that the numerical solutions show a monotonic decay as a function of λ, and the angle of the larger cone may have a slope of $\lambda^{1/3}$. Further study on the angle of the smaller cone and the asymptotic behavior of the solutions for $\lambda \to 0$ is in progress.

5. Summary

We have studied the evolution of a contracting or expanding bubble and the pinch-off of a viscous drop in axi-symmetric Stokes flows. The linear stability analysis suggests that an expanding bubble is stable while a contracting bubble is unstable to arbitrary axi-symmetric disturbances. Numerical computations show that an axi-symmetric bubble has the same behavior under large disturbances, though the growth of the instability is weakened by nonlinear effects. Numerical computations also suggest that, for a certain class of disturbances, a contracting bubble undergoes topological changes as different parts of the interface touch each other. This pinch-off appears to be a self-similar process, though the forms of the pinch-off depend on whether the pinch-off occurs as $z \to 0$ or $r \to 0$. For a viscous drop surrounded by another viscous fluid, it is found that the drop surface develops a canonical cone shape near pinch-off. The cone angles (for the wider cone) from our numerical simulations agree well with the physical experiment for large and medium-sized viscosity ratio λ. However, the difference between the physical experiments and numerical solutions are visible for very small λ.

Acknowledgments

We thank I. Cohen and J. Eggers for discussions and the experimental data. QN acknowledges partial support from NSF Grant DMS0074414. The work of ST was supported by NSF Grant DMS9803358 and DMS0103829. The work of TFD was supported primarily by the MRSEC Program of the National Science Foundation under Award Number DMR-9808595.

References

[1] H. A. Stone. Dynamics of drop deformation and breakup in viscous fluids. *Ann. Rev. Fluids Mech.*, 26:65–102, 1994.

[2] J. Eggers. Nonlinear dynamics and breakup of free-surface flows. *Reviews of Modern Physics*, 69(3):865, 1997.

[3] I. R. Grace R. Clift and M. E. Weber. *Bubbles, Drops and Particles*. Academic Press, 1977.

[4] Lord Rayleigh. On the stability of a cylinder of viscous fluid under a caplillary force. *Philos. Mag*, 34:145, 1892.

[5] J. M. Rallison and A. Acrivos. A numerical study of the deformation and burst of a viscous drop in an external flow. *J. Fluid Mech.*, 89:191–200, 1978.

[6] J. M. Rallision. The deformation of small viscous drops and bubbles in shear flows. *Ann. Rev. Fluids Mech.*, 16:45–66, 1984.

[7] C. Pozrikidis. The instability of a moving viscous drop. *J. Fluid Mech.*, 210:1–21, 1990.

[8] M. Manga and H. A. Stone. Buoyancy-driven interactions between two deformable viscous drops. *J. Fluid Mech.*, 256:647–683, 1993.

[9] T. M. Tsai and M. J. Miksis. Dynamics of a drop in a constricted capillary tube. *J. Fluid Mech.*, 274:197–217, 1994.

[10] J. Lister and H. Stone. Capillary breakup of a viscous thread surrounded by another viscous fluid. *Phys. Fluids*, 10:2759, 1998.

[11] S. Tanveer and G. Vasconcelos. Time-evolving bubbles in two-dimensional Stokes flow. *J. Fluid Mech.*, 301:325–344, 1995.

[12] S. Tanveer and G. Vasconcelos. Bubble breakup in two-dimensional stokes. *Rev. Lett.*, 73:2845–2848, 1994.

[13] C. Pozrikidis. Numerical studies of cusp formation at fluid interfaces in stokes flow. *J. Fluid Mech.*, 357:29–57, 1998.

[14] I. Cohen M. Brenner, J. Eggers and S. Nagel. Two fluid drop snal-off problem: experiments and theory. *Phy. Rev. Letter*, 83 (6):1147–1150, 1999.

[15] O. A. Ladyzhenskaya. *The mathematical theory of viscous incompressible flow*. Gordon and Breach, 1969.

[16] C. Pozrikidis. *Boundary integral and singularity methods for linearized viscous flow*. Cambridge University Press, 1992.

[17] H. T. Davis. *Introduction to nonlinear differential and Integral Equations*. Dover, 1962.

[18] Q. Nie and G. Baker. Application of adaptive quadrature to axi-symmetric vortex sheet motion. *J. of Comp. Physics*, 143:49–69, 1998.

[19] M. J. Shelley and G R. Baker. Order conserving approximation to derivatives of periodic function using iterated splines. *SIAM J. Num. Anal*, 25:1442, 1988.

[20] Y. Saad and M. H. Schultz. GMRES: A generalized minimal residual algorithm for nonsymmetric linear systems. *SIAM J. Sci. STat. Comput.*, 7:856–869, 1986.

[21] J. Hinch E. Kojima and A. Acrivos. The formation and expansion of a toroidal drop moving in a viscous fluid. *Phys. Fluids*, 27:19–32, 1984.

[22] Q. Nie and S. Tanveer. The evolution of an axi-symmetric stokes bubble with volumetric change. *IMA Preprint*, 1504, 1997.

[23] S. D. Howison and S. Richardson. Cusp development in free boundaries, and two-dimensional slow viscous flows. *Eur. J. Appl. Maths*, 6, 1995.

[24] Q. Nie and S. Tanveer. Self-similar break-up of a stokes bubble. *In Preparation*, 2001.

Department of Mathematics, University of California at Irvine, Irvine, CA 92697-3875

E-mail address: qnie@math.uci.edu

Department of Mathematics, Ohio State University, Columbus, OH 43210

E-mail address: tanveer@math.uci.edu

Department of Computer Science, University of Chicago, Chicago, IL 60637

E-mail address: dupont@cs.uchicago.edu

Department of Applied Mathematics, Illinois Institute of Technology, IL60616

E-mail address: lix@iit.edu